coatings

Article

Ab Initio Predicted Alloying Effects on the Elastic Properties of Al$_x$Hf$_{1-x}$NbTaTiZr High Entropy Alloys

Shaohui Li [1], Xiaodong Ni [1] and Fuyang Tian [1,2,*]

[1] Department of Physics, University of Science and Technology Beijing, Beijing 100083, China;
E-Mails: s20140993@xs.ustb.edu.cn (S.L.); nixd@ustb.edu.cn (X.N.)

[2] Applied Materials Physics, Department of Materials Science and Engineering, Royal Institute of Technology, Stockholm SE-100 44, Sweden

* Author to whom correspondence should be addressed; E-Mail: fuyang@ustb.edu.cn.

Academic Editor: T.M. Yue

Abstract: Using *ab initio* alloy theory, we investigate the equilibrium bulk properties and elastic mechanics of the single bcc solid-solution Al$_x$Hf$_{1-x}$NbTaTiZr (x = 0–0.7, 1.0) high entropy alloys. *Ab initio* predicted equilibrium volume is consistent with the available experiment. We make a detailed investigation of the alloying effect of Al and Hf on the equilibrium volume, elastic constants and polycrystalline elastic moduli. Results imply that the partial replacement Hf with Al increases the stability of the bcc phase and decreases the ductility of the Al$_x$Hf$_{1-x}$NbTaTiZr HEAs. The inner ductility of Al$_{0.4}$Hf$_{0.6}$NbTaTiZr is predicted by the calculations of ideal tensile strength.

Keywords: high-entropy alloys; *ab initio*; alloying effect; equilibrium bulk properties; elastic anisotropy; ideal tensile strength

1. Introduction

In the past decade, a simple solid-solution phase was found in a new alloy [1,2]. Yeh *et al.* named the new class of materials "high entropy alloys" (HEAs) [1]. HEAs are composed of at least five multiple principal elements in equimolar or near-equimolar ratios [1]. In spite of a considerable number of principal elements, some HEAs tend to form single-phase solid solution due to the small atomic size difference, high mixing entropy, and relatively low mixing enthalpy [3]. Single-phase HEAs adopt the

face-centered cubic (fcc) [1], body-centered cubic (bcc) [1] or Hexagonal Close-Packed (hcp) crystallographic structures [4]. Due to the unique microstructure, the excellently mechanical and corrosion resistant performances, HEAs, as the potential engineering materials, have attracted rapidly increasing attention in research community of materials and condensed physics.

The HEAs consisting of refractory elements satisfy the superior mechanical and functional properties in the high-temperature applications. Since the single bcc-phase WTaMoNb and WTaMoNbV HEAs were reported by Senkov *et al.*, many other experiments focus on the HEAs based on the refractory elements (Ti, Zr, Hf, V, Nb, Ta, Cr, Mo and W). For instance, the microstructures and mechanical properties were investigated for HfNbTaTiZr, HfTiZr, HfNbTiVZr and HfNbTiZr, *etc.* [5–8]. Due to the low density and similar atomic radius with the refractory elements (except for Cr), an Al element was used to dope refractory HEAs. Some researchers have investigated the effect of alloying with Al on the microstructure, composition and mechanical properties of these new refractory HEAs. For example, the addition of aluminum was found to increase hardness from 440.1 to 556.4 Hv as going from $MoNbTiV$ to $Al_{1.5}MoNbTiV$ [9]. The light-weight AlNbTiV has the specific yield strength, which can be comparable with strength of multi-phase refractory HEAs [10]. The Al additions have excellent beneficial effects on the microstructure and properties of parent $CrMo_{0.5}NbTa_{0.5}TiZr$ and HfNbTaTiZr [11]. For instance the hardness (yield strength) increases 3.8 to 4.9 GPa (929 to1841MPa) for HfNbTaTiZr and $Al_{0.4}Hf_{0.6}NbTaTiZr$.

Today, *ab initio* electronic structure methods have become powerful tools for predicting the atomic-level physical properties of multi-component metallic materials. However, HEAs present a great challenge for conventional *ab initio* calculations due to the complicated chemical and magnetic disorder. As an effective method to treat substitutional solid solutions, the exact muffin-tin orbital method in combination with the coherent potential approximation (EMTO-CPA) has been used to successfully predict the equilibrium bulk properties of some HEAs [12–14]. In the present work, we employ the EMTO-CPA *ab initio* density functional method to study the effect of Al addition on the equilibrium bulk properties and elastic parameters of $Al_xHf_{1-x}NbTaTiZr$ refractory HEAs.

The ideal strength provides the upper limit of the stress attainable during a specific loading condition, and is one of the importantly mechanical properties of metallic structure materials. For the calculations of ideal strength, there are often two special loading directions, such as ideal strength in tension, e.g., for cubic crystals under uniaxial load, and ideal strength in shear, e.g., for common slip systems (<111>{112} and <111>{110}) in the bcc crystal [15,16]. Due to the large strain behavior predicted from *ab initio*, researchers have investigated some elementary substances (Ti, Mo, Nb, V, W, Cu, Pt and Au *etc*.) and ordered alloys (TiAl and Ni_3Al) from *ab initio* calculations [16–19]. So far, the calculations of ideal strength of HEAs have not been found. In the present work, we investigate the ideal tensile strength of HEAs along bcc<001> direction.

The present theoretical predictions contribute to the further theoretical as well as experimental studies. The structure of this paper is as follows. In Section 2, we describe the computational tool and important numerical details. The equilibrium bulk properties, elastic mechanics and the ideal tensile strength are presented and discussed in Section 3. The paper ends with conclusions.

2. Computational Methods

The EMTO-CPA method is an efficient and accurate *ab initio* method for solving the Kohn-Sham (KS) equation in the density functional theory [20]. The exact one-electron potential is accurately discussed by using optimized overlapping muffin-tin potential. For total energy, the EMTO-CPA method uses the full charge density (FCD) technology [21–23], which improves the calculation efficiency and makes sure the accuracy is similar to the full-potential methods. Nowadays, CPA is the most effective alloy theory for calculating electronic structure in multi-component random solid solutions [24–28], despite of the single-site nature of the CPA limiting its applicability to system with insignificant short-range order and local lattice relaxation effects. It has been proven that using the EMTO-CPA method can obtain the structural energy differences related to the lattice distortion in complex alloys of arbitrary number of components and compositions [29–34].

In the present calculations, we used Local Density Approximation (LDA) density function to solve the KS equation within the scalar-relativistic approximation [35]. The Green's function was calculated for 16 complex energy points including the valence states. The EMTO basis set included s, p, d, and f states. The irreducible wedge of the bcc Brillouin zone was sampled by 285 inequivalent k points. The electrostatic correction to the single-site CPA was described using the screened impurity model [36]. According to the standard methodology and the Viogt-Reuss-Hill averaging method [37], the three independent single-crystal cubic elastic constants (c_{11}, c_{12}, c_{44}) and the polycrystalline elastic moduli (B, G, E, v) were obtained. For all alloy components, the potential sphere radii were chosen to be equal to the corresponding average atomic sphere radius. All calculations were performed for a static lattice (that is, neglecting all thermal contributions).

In the calculations of ideal tensile strength, the stress σ is given by [38]

$$\sigma(\varepsilon) = \frac{1+\varepsilon}{V(\varepsilon)} \frac{\partial E}{\partial \varepsilon} \tag{1}$$

where E is the total energy per atom and V is volume per atom at a given tensile strain. ε denotes the train of the simulation cell in the direction of the applied uniaxial force. It is defined as

$$\varepsilon = \frac{l_{\parallel} - l_0}{l_0} \tag{2}$$

where $l_{\parallel}$ and l_0 is the length of the cell along the direction of uniaxial stress in the final state and in the initial state, respectively.

The uniaxial tensile stress is loaded along bcc<001> direction to obtain energy difference and relevant strain. In this work, we only consider the uniaxial tensile stress of $Al_{0.4}Hf_{0.6}NbTaTiZr$ along the Bain path.

3. Results and Discussion

3.1. Equilibrium Volume

Experiments indicated that $Al_{0.4}Hf_{0.6}NbTaTiZr$ and $HfNbTaTiZr$ adopt single-phase bcc structure [11]. It is noted that Ti, Zr and Hf are stable in the hexagonal close packed (hcp) phase at ambient conditions,

whereas these refractory elements become bcc phase at elevated temperature. In this part, we firstly study the atomic Wigner-Seitz (WS) radius and bulk modulus of each alloying element, and then turn to the Al$_x$Hf$_{1-x}$NbTaTiZr HEAs. In Table 1, we list theoretically calculated WS radii and the bulk moduli along with the available experiment data [28]. Here w_t and w_e represent the theoretical (EMTO) WS radius and experimental WS radius of alloy elements and HEAs respectively. B_t and B_e are the theoretical and experimental bulk moduli of the alloy elements. We can see from Table 1 that the theoretical results and experimental data are in good agreement with each other. The relative deviations of all elements between calculations and experiments are within the range of the errors obtained within the present density function approximation [35].

For HEAs, Table 1 shows the theoretical equilibrium WS radius. Unfortunately, the experimental equilibrium WS radii are only available to Al$_x$Hf$_{1-x}$NbTaTiZr (x = 0, 0.4) [11,39]. With the increase of Al content, the theoretical WS radius of HEAs decreases from 3.216 to 3.127 Bohr, which is in line with the trend of experimental WS radius measured by x-ray diffraction. The symbol Δ stands for the relative deviation (in %) between the theoretical and experimental WS radius. The Δ is about 1.5% for Al$_x$Hf$_{1-x}$NbTaTiZr (x = 0, 0.4). These small errors might be due to the effect of temperature neglected in the present calculations. Although the similar measure method was employed, the experimental Wigner-Seitz radius w = 3.168 Bohr from Reference [11] is smaller than w = 3.178 Bohr from Ref [39]. To further assess the theoretical equilibrium WS radii, we make use of Vegard's law to estimate the equilibrium WS radius by using the WS radius of the alloy components. In Table 1, $\overline{w}_t$ stands for the estimated radius based on the present theoretical values and $\overline{w}_e$ is the one obtained from the experimental data. As expected, $\overline{w}_t$ and $\overline{w}_e$ agree with each other. Both $\overline{w}_t$ and $\overline{w}_e$ are slightly smaller than w_t. For all HEAs considered here, the results show a systematic negative deviation relative to Vegard's rule.

The atomic size difference is one of important parameters that are used to determine the formation of the solid solution phases [40,41]. The atomic size difference parameter δ is defined as

$$\delta = 100\sqrt{\sum\nolimits_{i=1}^{n} c_i \left(1 - r_i / \overline{r}\right)^2} \qquad (3)$$

where $\overline{r} = \sum\nolimits_{i=1}^{n} c_i r_i$, with r_i and c_i being the atomic radius and atomic percentage of the individual alloy components, respectively, and n the number of components. For the solid solutions with bcc crystals, δ should be smaller than 8.5 from Ref [40] and 6.6 from Ref [41]. Here, we estimate δ from the WS radii of alloying elements. In Table 1, for all HEAs, δ_t derived from the *ab initio* calculations is very close to δ_e obtained from experiments. Both δ_t and δ_e are below 6.6%, which are in line with the rule of single-phase solid solutions with bcc phase [3,40,41]. As an indicator to determine the crystals of single-phase solid solutions, the valence electron concentration is often used to predict the solid solution phase of HEAs. According to statistical law [3], HEAs with valence electron concentration (VEC) < 7.5 adopt the bcc phase. VEC of the present HEAs is about 4.2–4.4, which remains below the phenomenological threshold value.

Table 1. WS radii (*w*, units of Bohr) for the pure metals (M) in their equilibrium crystal structure and for $Al_xHf_{1-x}NbTaTiZr$ in the bcc structure shown as a function of Al content. w_t and w_e represent the theoretical (EMTO) and the experimental WS radius, respectively, B_t is calculated bulk modulus, B_e is the experimental one. *VE* stands for the number of valence electrons. $\overline{w_t}$ and $\overline{w_e}$ are the estimated WS radii of the HEAs from w_t and w_e values of pure metal elements, respectively, according to Vegard's rule. Δ stands for the relative deviation (in %) between the theoretical and experimental data, $δ_t$ and $δ_e$ are the WS radius differences (in %) obtained from theoretical and experimental WS radii according to Equation (3); VEC is the valence electron concentration obtained via $VEC = \sum_{i=1}^{n} c_i e_i$, where e_i is the number of valence electrons and c_i the atomic fraction of alloy component *i*.

M	w_t	B_t	w_e	B_e	VE	x	w_t	w_e	Δ	$\overline{w_t}$	$\overline{w_e}$	$δ_t$	$δ_e$	VEC
Al	2.965	84	2.991	73	3	0	3.216	3.168 [a]	1.52 [a]	3.216	3.169	5.0	4.3	4.40
Hf	3.402	142	3.301	108	4	–	–	3.178 [b]	1.20 [b]	–	–	–	–	–
Nb	3.119	178	3.071	169	5	0.1	3.208	–	–	3.206	3.163	5.0	–	4.38
Ta	3.113	223	3.073	191	5	0.2	3.199	–	–	3.196	3.157	5.0	–	4.36
Ti	3.030	133	3.053	106	4	0.3	3.190	–	–	3.186	3.150	5.0	–	4.34
Zr	3.368	74	3.347	95	4	0.4	3.181	3.134	1.50	3.176	3.144	5.0	4.3	4.32
–	–	–	–	–	–	0.5	3.172	–	–	3.166	3.138	5.0	–	4.30
–	–	–	–	–	–	0.6	3.163	–	–	3.156	3.132	4.9	–	4.28
–	–	–	–	–	–	0.7	3.154	–	–	3.146	3.126	4.8	–	4.26
–	–	–	–	–	–	1.0	3.127	–	–	3.116	3.107	4.4	–	4.20

[a] Experiment, Reference [11]; [b] Experiment, Reference [39].

3.2. Cubic Elastic Constants

The elastic constants c_{11}, c_{12} and c_{44} as well as the Zener ratio A_z, the Cauchy pressure ($c_{12}–c_{44}$) and the tetragonal shear modulus c' of $Al_xHf_{1-x}NbTaTiZr$ are listed in Table 2. The elastic constants (c_{11}, c_{12}, c_{44}, ($c_{12}–c_{44}$) and A_z) of $Al_xHf_{1-x}NbTaTiZr$ are plotted in Figure 1 as a function of Al content.

Table 2. Theoretical elastic constants c_{11}, c_{12}, c_{44}, c' (units of GPa), polycrystalline elastic moduli *B*, *G*, *E* (unit of GPa) as well as the *B/G* ratio, the Zener ratio A_z, the elastic anisotropy ratio A_{VR}, the Poisson's ratio v and Cauchy pressure ($c_{12}–c_{44}$) (unit of GPa) for the body-centered cubic (bcc) phase $Al_xHf_{1-x}NbTaTiZr$ HEAs (*x* = 0–0.7,1).

| x	B	c_{11}	c_{12}	c_{44}	G	B/G	E	v	c'	$c_{12}–c_{44}$	A_{VR}	A_Z
0	134.0	158.1	121.9	62.2	38.03	3.523	104.2	0.370	18.1	59.7	0.1713	3.431
0.1	135.6	160.9	123.0	62.6	38.84	3.492	106.4	0.369	18.9	60.4	0.1620	3.309
0.2	137.0	163.1	123.9	63.1	39.55	3.464	108.2	0.368	19.6	60.8	0.1552	3.220
0.3	138.5	165.5	125.0	63.6	40.25	3.442	110.1	0.368	20.2	61.4	0.1494	3.146
0.4	140.0	167.7	126.1	64.2	40.92	3.420	111.9	0.367	20.8	61.9	0.1451	3.091
0.5	141.7	170.1	127.5	64.9	41.57	3.408	113.6	0.366	21.3	62.6	0.1418	3.049
0.6	143.3	172.3	128.9	65.7	42.18	3.398	115.2	0.366	21.7	63.2	0.1401	3.028
0.7	144.8	174.3	130.0	66.7	42.89	3.376	117.1	0.365	22.1	63.3	0.1394	3.019
1.0	149.7	180.4	134.3	70.0	44.94	3.331	122.6	0.364	23.1	64.3	0.1407	3.035

The dynamical stability condition is satisfied by the theoretical single-crystal elastic constants for the present HEAs, *i.e.*, $c_{44} > 0$, $c_{11} > |c_{12}|$ and $c_{11} + 2c_{12} > 0$ [37]. From Table 2, we can see that all HEAs considered here are mechanically stable. As shown in Figure 1, the partial replacement of Hf with Al in $Al_xHf_{1-x}NbTaTiZr$ ($x = 0$–0.7, 1) HEAs slightly increases the tetragonal elastic constant c' with the increase of Al content. The trend implies that Al enhances the mechanical stability of the bcc phase against tetragonal deformation for the present HEAs. The positive Cauchy pressure (c_{12}–c_{44}) is associated with the covalent nature of the metallic bond and the character of ductile alloy [42]. Due to the large positive Cauchy pressure (c_{12}–c_{44}) shown in Figure 1, the present HEAs are predicted to have a strong metallic character and good ductility. We observe that the Cauchy pressure (c_{12}–c_{44}) slightly increases with the addition of Al content.
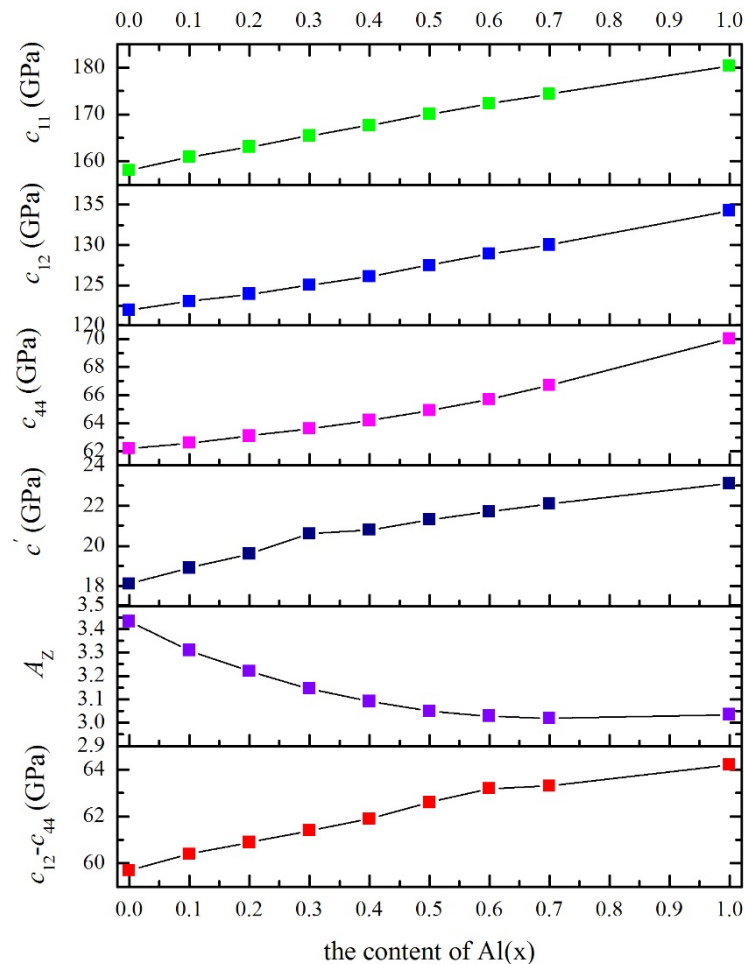
Figure 1. Theoretical elastic constants of $Al_xHf_{1-x}NbTaTiZr$ as a function of Al content.

3.3. Polycrystalline Elastic Moduli

Table 2 shows the polycrystalline elastic moduli, including the bulk modulus *B*, the shear modulus *G*, Young's modulus *E* and the Poisson ratio *v* as well as the Pugh ratio *B/G* and elastic anisotropy ratio A_{VR} of $Al_xHf_{1-x}NbTaTiZr$. The theoretical results for $Al_xHf_{1-x}NbTaTiZr$ are plotted in Figure 2.
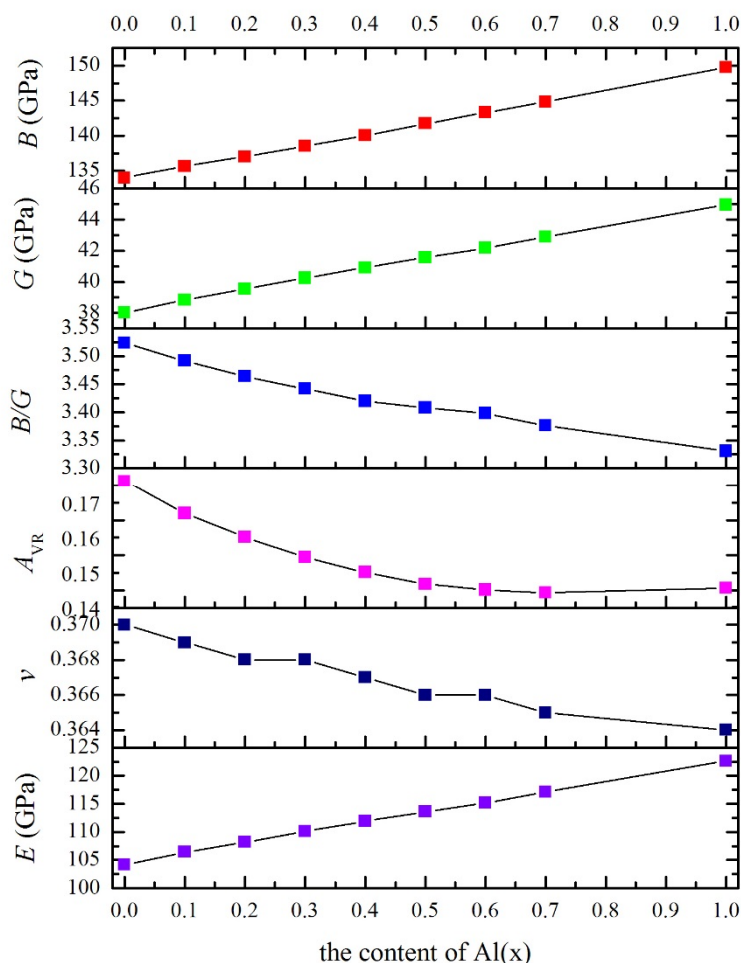
Figure 2. Polycrystalline elastic moduli for Al$_x$Hf$_{1-x}$NbTaTiZr as a function of Al content.

To our knowledge, there are is available experimental information on the polycrystalline elastic moduli of the Al$_x$Hf$_{1-x}$NbTaTiZr HEAs, expect for Al$_{0.4}$Hf$_{0.6}$NbTaTiZr [11] and HfNbTaTiZr [39]. For the present HEAs, the bulk modulus *B* changes from 134.0 to 149.7 GPa, *G* from 38.0 to 44.9 GPa, *E* from 104.2 to 122.6 GPa. The partial replacement Hf with Al increases these polycrystalline elastic moduli. For the ductile–brittle behavior of alloys, *B/G* is one of indexes [43]. Generally the materials with *B/G* > 1.75 are ductile, whereas those with *B/G* < 1.75 are considered to be brittle. According to Table 2 and Figure 2, the Pugh ratio *B/G* is larger than the critical value 1.75 for the present HEAs. The Poisson ratio *v* is considered as an indicator to predicate the ductile-brittle behavior of metallic materials. In some literature, bulk metal glasses are reported to have good ductility with the *v* > 0.31 [44]. The Poisson ratio of the present HEAs is *v* = 0.36–0.37. Combining *B/G* and *v*, we find that the Al$_x$Hf$_{1-x}$NbTaTiZr HEAs are predicted to be ductile, and the ductility slightly decreases with the increase of Al content. It should be noted that these phenomenological correlations between elastic moduli and the ductile/brittle behavior of materials have not been confirmed in the case of HEAs.

The Zener ratio *A$_Z$* (*c$_{44}$/c′*) and the elastic anisotropy ratio *A$_{VR}$* are used to predict the elastic anisotropy of materials. For instance, *A$_Z$* = 1 and *A$_{VR}$* = 0 correspond to the elastically isotropic materials. The Zener ratio *A$_Z$* > 1 shown in Table 2 implies that the present HEAs are anisotropic. From Figure 2 we can see that partial substitution of Hf with Al has a small effect on the elastic anisotropy of Al$_x$Hf$_{1-x}$NbTaTiZr HEAs. With increasing of Al content, *A$_Z$* decreases from 3.431 to 3.035 and *A$_{VR}$* is from 0.1713 to

0.1407. Due to the anisotropy, the Young's modulus changes with the crystalline direction. For the cubic crystal, the Zener ratio $A_Z > 1$ implies that the largest (smallest) Young's modulus is along the <111>(<001>) crystalline direction. For instance for $Al_{0.4}Hf_{0.6}NbTaTiZr$ the Young's modulus E are 167 GPa, 59.5 GPa and 115GPa along <111>, <001> and <110> crystalline directions, respectively. Our calculated average Young's modulus E = 111.9 GPa is slightly large, comparing with the experimental E = 78.1 GPa at room temperature [11]. The large deviation is between our calculated E = 104.2 GPa and the experimental $E \approx 55$ GPa [39] for HfNbTaTiZr. It should be emphasized that all present calculations were carried out at static conditions (0 K) and the present HEAs are assumed an ideal solid solution phase with bcc underlying lattice.

3.4. The Ideal Tensile Strength of $Al_{0.4}Hf_{0.6}NbTaTiZr$

As an inherent property of a material, the ideal tensile strength (ITS) does not change with the grain boundaries, cracks, dislocations, and microstructural defects, ITS offers insight into the correlation between the intrinsic chemical bonding and the crystal symmetry [45]. Figure 3 shows the energy difference ΔE and stress σ as a function of relaxed tensile strain and unrelaxed tensile strain along bcc<001> direction, respectively. We can see from Figure 3 that the relaxed (unrelaxed) maximum stress is 3.86 (4.20) GPa at the critical strain of ε = 10.6% (10.4%), which is bigger than the experimental value of the 2.27 GPa at the strain ε = 10%. The reason for the phenomenon may be that the experiment-measured value is the strength of real crystal, considering the crystal dislocation and temperature in the process of measurement. Owing to the Poisson contraction, the relaxed strain ε = 27.0%, leading to formation of an fcc structure (the second zero-stress point), is smaller than the unrelaxed one of 27.5%. The energy curve shown in Figure 3 implies that the deformation of the cubic structure is unstable at ε = 27.0% [46]. With further increase of the strain, a stress-free tetragonal structure is reached at the strain of 32.7%, which is in line with the third zero-stress point in the stress-strain curve. For the unrelaxed strain, the third zero-stress point is ε = 32.3%.
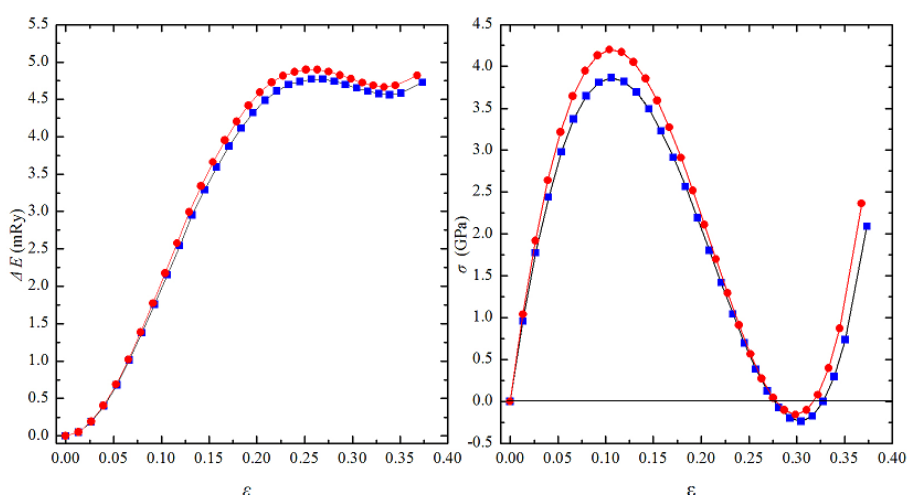
Figure 3. The energy difference ΔE and tensile stress σ as a function of tensile strain ε under <001> tensile loading for $Al_{0.4}Hf_{0.6}NbTaTiZr$. The rectangles stand for ΔE and σ of the relaxed structure, the cycles represent ΔE and σ of the unrelaxed structure.

4. Conclusions

We employed the *ab initio* EMTO-CPA method to study the equilibrium bulk properties, elastic parameters and ideal tensile strength of $Al_xHf_{1-x}NbTaTiZr$ ($x = 0–1$) HEAs. The calculated equilibrium volumes are consistent with available experimental data and the estimated Wigner-Seitz radii. According to the atomic size difference and valence electron concentration, the present HEAs adopt a single-phase bcc crystalline structure. The trends of the calculated elastic parameters imply that the addition of Al increases the thermodynamic stability of the bcc phase of the present HEAs.

According to the *ab initio* B/G ratio and Poisson ratio v, theoretical calculations suggested that the ductility of the present HEAs slightly decreases with the increasing Al content, whereas all HEAs remain ductile. The anisotropic $Al_xHf_{1-x}NbTaTiZr$ HEAs are predicted from the criteria of Zener ratio and polycrystalline elastic ratio. Furthermore, the change of Young's moduli E is from 59.5 GPa to 160 GPa along the different crystalline directions. Considering the effect of temperature, our *ab initio* calculated $E = 111.9$ GPa is acceptable compared to the experimental $E = 78.1$ GPa at room temperature. For the ideal tensile strength of $Al_{0.4}Hf_{0.6}NbTaTiZr$, the maximum stress is 3.85 GPa at the critical strain of $\varepsilon = 10.6\%$.

Author Contributions

Fuyang Tian and Shaohui Li designed the research; Shaohui Li performed the calculations and analyzed the data; Shaohui Li, Xiaodong Ni and Fuyang Tian wrote the paper.

Conflicts of Interest

The authors declare no conflict of interest.

References

1. Yeh, J.W.; Chen, S.K.; Lin, S.J.; Gan, J.Y.; Chin, T.S.; Shun, T.T.; Chang, S.Y. Nanostructured high-entropy alloys with multiple principal elements: Novel alloy design concepts and outcomes. *Adv. Eng. Mater.* **2004**, *6*, 299–303.
2. Cantor, B.; Chang, I.T.H.; Knight, P.; Vincent, A.J.B. Microstructural development in equiatomi multicomponent alloys. *Mater. Sci. Eng. A* **2004**, *375–377*, 213–218.
3. Tian, F.; Varga, L.K.; Chen, N.; Shen, J.; Vitos, L. Empirical design of single phase high-entropy alloys with high hardness. *Intermetallics* **2015**, *58*, 1–6.
4. Takeuchi, A.; Amiya, K.; Wada, T.; Yubuta, K.; Zhang, W. High-entropy alloys with a hexagonal close-packed structure designed by equi-atomic alloy strategy and binary phase diagrams. *JOM* **2014**, *66*, 1984–1992.

5. Senkov, O.N.; Scott, J.M.; Senkova, S.V.; Miracle, D.B.; Woodward, C.F. Microstructure and room temperature properties of a high-entropy TaNbHfZrTi alloy. *J. Alloys Compd.* **2011**, *509*, 6043–6048.

6. Guo, W.; Dmowski, W.; Noh, J.-Y.; Rack, P.; Liaw, P.K.; Egami, T. Local atomic structure of a high-entropy alloy: An X-ray and neutron scattering study. *Metall. Mater. Trans. A* **2012**, *44*, 1994–1997.

7. Fazakas, É.; Zadorozhnyy, V.; Varga, L.K.; Inoue, A.; Louzguine-Luzgin, D.V.; Tian, F.; Vitos, L. Experimental and theoretical study of $Ti_{20}Zr_{20}Hf_{20}Nb_{20}X_{20}$ (X = V or Cr) refractory high-entropy alloys. *Int. J. Refract. Met. Hard Mater.* **2014**, *47*, 131–138.

8. Wu, Y.D.; Cai, Y.H.; Wang, T.; Si, J.J.; Zhu, J.; Wang, Y.D. A refractory $Hf_{25}Nb_{25}Ti_{25}Zr_{25}$ high-entropy alloy with excellent structural stability and tensile properties. *Mater. Lett.* **2014**, *130*, 277–280.

9. Chen, S.; Yang, X.; Dahmen, K.; Liaw, P.; Zhang, Y. Microstructures and crackling noise of Al_xNbTiMoV high entropy alloys. *Entropy* **2014**, *16*, 870–884.

10. Stepanov, N.D.; Shaysultanov, D.G.; Salishchev, G.A.; Tikhonovsky, M.A. Structure and mechanical properties of a light-weight AlNbTiV high entropy alloy. *Mater. Lett.* **2015**, *142*, 153–155.

11. Senkov, O.N.; Senkova, S.V.; Woodward, C. Effect of aluminum on the microstructure and properties of two refractory high-entropy alloys. *Acta Mater.* **2014**, *68*, 214–228.

12. Tian, F.; Varga, L.K.; Chen, N.; Delczeg, L.; Vitos, L. *Ab initio* investigation of high-entropy alloys of 3D elements. *Phys. Rev. B* **2013**, *87*, doi:10.1103/PhysRevB.87.075144.

13. Tian, F.; Delczeg, L.; Chen, N.; Varga, L.K.; Shen, J.; Vitos, L. Structural stability of $NiCoFeCrAl_x$ high-entropy alloy from *ab initio* theory. *Phys. Rev. B* **2013**, *88*, doi:10.1103/PhysRevB.88.085128.

14. Tian, F.; Varga, L.K.; Chen, N.; Shen, J.; Vitos, L. *Ab initio* design of elastically isotropic $TiZrNbMoV_x$ high-entropy alloys. *J. Alloys Compd.* **2014**, *599*, 19–25.

15. Černý, M.; Šob, M.; Pokluda, J.; Šandera, P. *Ab initio* calculations of ideal tensile strength and mechanical stability in copper. *J. Phys. Condens. Matter.* **2004**, *16*, doi:10.1088/0953-8984/16/7/004.

16. Nagasako, N.; Jahn´atek, M.; Asahi, R.; Hafner, J. Anomalies in the response of V, Nb, and Ta to tensile and shear loading: *Ab initio* density functional theory calculations. *Phys. Rev. B* **2010**, *81*, doi:10.1103/PhysRevB.81.094108.

17. Wang, Y.J.; Wang, C.Y. A comparison of the ideal strength between $L1_2Co_3(Al,W)$ and Ni_3Al under tension and shear from first-principles calculations. *Appl. Phys. Lett.* **2009**, *94*, doi:10.1063/1.3170752.

18. Zhou, H.B.; Zhang, Y.; Liu, Y.L.; Kohyama, M.; Yin, P.G.; Lu, G.H. First-principles characterization of the anisotropy of theoretical strength and the stress-strain relation for a TiAl intermetallic compound. *J. Phys. Condens. Matter.* **2009**, *21*, doi:10.1088/0953-8984/21/17/175407.

19. Černý, M.; Pokluda, J. Ideal tensile strength of cubic crystals under superimposed transverse biaxial stresses from first principles. *Phys. Rev. B* **2010**, *82*, doi:10.1103/PhysRevB.82.174106.

20. Kohn, W.; Sham, L.J. Self-consistent equations including exchange and correlation effects. *Phys. Rev.* **1965**, *140*, 1133–1138.

21. Vitos, L. Total-energy method based on the exact muffin-tin orbitals theory. *Phys. Rev. B* **2001**, *64*, doi:10.1103/PhysRevB.64.014107.

22. Kollár, J.; Vitos, L.; Skriver, H.L. Surface energy and work function of the light actinides. *Phys. Rev. B* **1994**, *49*, doi:10.1103/PhysRevB.49.11288.

23. Vitos, L.; Kollár, J.; Skriver, H.L. Full charge-density calculation of the surface energy of metals. *Phys. Rev. B* **1994**, *49*, doi:10.1103/PhysRevB.49.16694.

24. Stocks, G.M.; Temmerman, W.M.; Gyorffy, B.L. Complete solution of the korringa-kohn-rostoker coherent-potential-approximation equations: Cu-Ni alloys. *Phys. Rev. Lett.* **1978**, *41*, 339–343.

25. Johnson, D.D.; Nicholson, D.M.; Pinski, F.J.; Gyorffy, B.L.; Stocks, G.M. Density-functional theory for random alloys: Total energy within the coherent-potential approximation. *Phys .Rev. Lett.* **1986**, *56*, 2088–2091.

26. Vitos, L.; Abrikosov, I.A.; Johansson, B. Anisotropic lattice distortions in random alloys from first-principles theory. *Phys. Rev. Lett.* **2001**, *87*, doi:10.1103/PhysRevLett.87.156401.

27. Gyorffy, B.L. Coherent-potential approximation for a non-overlapping-muffin-tin-potential model of random substitutional alloys. *Phys. Rev. B* **1972**, *5*, 2382–2384.

28. Vitos, L. *The Emto Method and Applications in Computational Quantum Mechanics for Materials Engineers*; Springer-Verlag: London, UK, 2007.

29. Vitos, L.; Korzhavyi, P.A.; Johansson, B. Elastic property maps of austenitic stainless steels. *Phys. Rev. Lett.* **2002**, *88*, doi:10.1103/PhysRevLett.88.155501.

30. Taga, A.; Vitos, L.; Johansson, B.; Grimvall, G. *Ab initio* calculation of the elastic properties of $Al_{1−x}Li_x(x \leq 0.20)$ random alloys. *Phys. Rev. B* **2005**, *71*, doi:10.1103/PhysRevB.71.014201.

31. Huang, L.; Vitos, L.; Kwon, S.K.; Johansson, B.; Ahuja, R. Thermoelastic properties of random alloys from first-principles theory. *Phys. Rev. B* **2006**, *73*, 104203–104207.

32. Vitos, L.; Korzhavyi, P.A.; Johansson, B. Evidence of large magnetostructural effects in austenitic stainless steels. *Phys. Rev. Lett.* **2006**, *96*, doi:10.1103/PhysRevLett.96.117210.

33. Vitos, L.; Johansson, B. Large magnetoelastic effects in paramagnetic stainless steels from first principles. *Phys. Rev. B* **2009**, *79*, doi:10.1103/PhysRevB.79.024415.

34. Zhang, H.; Punkkinen, M.P.J.; Johansson, B.; Hertzman, S.; Vitos, L. Single-crystal elastic constants of ferromagnetic bcc Fe-based random alloys from first-principles theory. *Phys. Rev. B* **2010**, *81*, doi:10.1103/PhysRevB.81.184105.

35. Perdew, J.P.; Burke, K.; Ernzerhof, M. Generalized gradient approximation made simple. *Phys. Rev. Lett.* **1996**, *77*, 3865–3868.

36. Korzhavyi, P.A.; Ruban, A.V.; Abrikosov, I.A.; Skriver, H.L. Madelung energy for random metallic alloys in the coherent potential approximation. *Phys. Rev. B* **1995**, *51*, 5773–5780.

37. Grimvall, G. *Thermophysical Properties of Materials*; North-Holland: Amsterdam, The Netherland, 1999.

38. Roundy, D.; Krenn, C.R.; Cohen, M.L.; Morris, J.W. The ideal strength of tungsten. *Philos. Mag. A* **2001**, *81*, 1725–1747.

39. Lin, C.M.; Juan, C.C.; Chang, C.H.; Tsai, C.W.; Yeh, J.W. Effect of Al addition on mechanical properties and microstructure of refractory Al_xHfNbTaTiZr alloys. *J. Alloys Compd.* **2015**, *624*, 100–107.

40. Guo, S.; Liu, C.T. Phase stability in high entropy alloys: Formation of solid-solution phase or amorphous phase. *Prog. Nat. Sci. Mater. Int.* **2011**, *21*, 433–446.

41. Yang, X.; Zhang, Y. Prediction of high-entropy stabilized solid-solution in multi-component alloys. *Mater. Chem. Phys.* **2012**, *132*, 233–238.

42. Nguyen-Manh, D.; Mrovec, M.; Fitzgerald, S.P. Dislocation driven problems in atomistic modelling of materials. *Mater. Trans.* **2008**, *49*, 2497–2506.

43. Pugh, S.F. Relations between the elastic moduli and the plastic properties of polycrystalline pure metals. *Philos. Mag.* **1954**, *45*, 823–843.

44. Gu, X.J.; McDermott, A.G.; Poon, S.J.; Shiflet, G.J. Critical Poisson's ratio for plasticity in Fe-Mo-C-B-Ln bulk amorphous steel. *Appl. Phys. Lett.* **2006**, *88*, doi:10.1063/1.2206149.

45. Clatterbuck, D.M.; Chrzan, D.C.; Morris, J.W. The ideal strength of iron in tension and shear. *Acta. Mater.* **2003**, *51*, 2271–2283.

46. Craievich, P.J.; Weinert, M.; Sanchez, J.M.; Watson, R.E. Local stability of nonequilibrium phases. *Phys. Rev. Lett.* **1994**, *72*, 3076–3079.